The evolution of isolated cavities and hydraulic connection at the glacier bed. Part 2: a dynamic viscoelastic model

Christian Schoof[1]

[1]Department of Earth, Ocean and Atmospheric Sciences, University of British Columbia, Vancouver, BC, Canada
Correspondence to: C. Schoof (cschoof@mail.ubc.ca)

Abstract. Many large-scale subglacial drainage models assume implicitly or explicitly that the distributed part of the drainage system consists of subglacial cavities. Few of these models however consider the possibility of hydraulic disconnection, where cavities exist but are not numerous or large enough to be pervasively connected with one another so that water can flow. Here I use a process-scale model for subglacial cavities to explore their evolution, focusing on the dynamics of connections that are made between cavities. The model uses a viscoelastic representation of ice, and computes the pressure gradients that are necessary to move water around basal cavities as they grow or shrink. The latter model component sets the work here apart from previous studies of subglacial cavities, and permits the model to represent the behaviour of isolated cavities, and of uncavitated parts of the bed at low normal stress. I show that connections between cavities are made dynamically when a cavitation ratio (the fraction of the bed occupied by cavities) reaches a critical value due to decreases in effective pressure. I also show that existing simple models for cavitation ratio and for water sheet thickness (defined as mean water depth) fail to capture even qualitatively the behaviour predicted by the present model.

1 Introduction

Much of the interest in subglacial drainage is motivated by the effect of pressureized subglacial water on glacier sliding (Iken and Bindschadler, 1986): basal friction is reduced when basal water pressure is high, or more precisely, when basal effective pressure is low. The relationship between effective pressure and basal friction is called the basal friction law: a parameterization that computes mean basal drag as a function of basal effective pressure, sliding velocity and possibly other variables that can be computed by a large-scale model. First-principles derivations of friction laws (e.g. Weertman, 1957; Nye, 1969; Kamb, 1970; Fowler, 1981, 1986; Schoof, 2005; Gagliardini et al., 2007; Helanow et al., 2020, 2021) average stresses over a local process scale, such as that involved in the ploughing of clasts through till or the flow of ice over bed obstacles, to compute mean drag at the glacier bed.

The basal effective pressure that appears in the friction law is likewise defined as an average of the difference between local normal stress at the bed and basal water pressure. At the local process scale, actual normal stresses are heterogeneous but have a well-defined average that is generally close to local ice overburden. By contrast, basal water pressure is generally not assumed to be heterogeneous. A spatially smoothly-varying basal water pressure will result if there is a pervasive, connected subglacial drainage system that causes pressure differences to equilibrate rapidly.

A growing body of observational evidence however suggests that hydraulic isolation of significant parts of glacier beds is a common phenomenon, even during the summer melt season. Moreover, different parts of the glacier bed can switch back and forth between being connected and isolated (Fudge et al., 2008; Andrews et al., 2014; Rada and Schoof, 2018). While not included in most of the current generation of widely-used subglacial drainage models (Werder et al., 2013; Sommers et al.,

5   2018), there have been some recent attempts to account for hydraulic isolation (Hoffman et al., 2016; Rada and Schoof, 2018). In the framework of modern, "distributed" drainage models, dynamic changes in connectivity have to be formulated on the primary model variables, usually effective pressure N and a mean ice-bed gap width (pr "water sheet thickness") $\bar{h}$. The model in Rada and Schoof (2018) uses a discrete network formulation, but its distributed equivalent is a distributed water model (Hewitt, 2011, 2013; Schoof et al., 2012; Werder et al., 2013) in which hydraulic connection is established if sheet thickness $\bar{h}$

10   exceeds a threshold h_c. That is, a finite water flux through the sheet occurs if

$$\bar{h} > h_c, \tag{1}$$

and $\bar{h}$ is usually assumed to evolve according to a model of the form (Hewitt, 2011; Schoof et al., 2012)

$$\frac{\partial \bar{h}}{\partial t} = v_o(\bar{h}, u_b) - v_c(\bar{h}, N), \tag{2}$$

Here, u_b is sliding velocity and v_o represents opening of the water sheet due to sliding over bed roughness, while v_c is a creep

15   closure term. (Note that most drainage models dispense with the overbar on $\bar{h}$; I retain it here because I reserve h for the *local* ice-bed gap width later.)

The justification for such a treatment of hydraulic connection is that small cavities can exist in the lee of bed bumps without being sufficiently connected to each other to allow water flow, as in a percolation problem (Hammersley and Welsh, 1980). While appealing, this simple treatment has not been tested against a process-scale model of subglacial cavity formation. In

20   fact, existing models of cavity formation (Fowler, 1986; Schoof, 2005; Gagliardini et al., 2007; Helanow et al., 2020, 2021; Stubblefield et al., 2021; de Diego et al., 2021, 2022) generally assume that the underlying bed itself is highly permeable and provides easy access for water to be injected into any part of the bed where normal stress in the ice has dropped to the water pressure in an ambient (but not otherwise modelled) drainage system.

The present paper is part of an effort to dispense with that assumption of a perfectly permeable bed, and study instead how

25   cavities can expand dynamically along the ice-bed interface from an access point where water is injected at prescribed pressure by an ambient drainage system. In a companion paper (Schoof, submitted), henceforth referred to as part 1, I have used a modification of existing steady state cavity models in two dimensions to study cavity expansion under quasi-steady conditions. That is, part 1 assumes an ambient drainage system with a prescribed effective pressure N that varies slowly enough for the cavity roof to be always in a steady state.

30   Based on that assumption, part 1 shows that connections between the ambient drainage system and previously uncavitated parts of the bed are made in a quasi-steady state at a set of critical effective pressures. The system of cavities also exhibits hysteresis. If cavity enlargement has occurred previously and cavity size has shrunk subsequently due to an increase in ambient effective pressure, then reconnection to the now isolated pre-existing cavities happens at a different set of higher effective pressure: reconnecting to an existing cavity is easier than creating a new cavity.
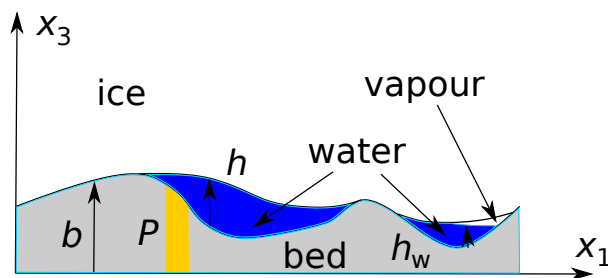
Figure 1. Definitions used in the paper. Beige colour is used throughout the paper to indicate the connection portions P of the bed. h is used here to denote the ice-bed gap, which will often be equal to water depth h_w, but can differ if water pressure vanishes, and a partially vapour-filled cavity forms.

In a time-dependent system, cavity connections are likely to be more complicated than the quasi-steady model suggests. To study dynamic cavity connections, I complement the work in part 1 with a generalized dynamic model. Ice is treated as viscoelastic to account for the possibility that cavity expansion could be very rapid, and occur on time scales that are short compared with the Maxwell time of ice. In addition, I account explicitly for the water pressure gradients that are necessary

5 to move water around a cavity, and in particular, into any ice-bed gaps that are newly created when rapid cavity enlargements occur. By using a mass conservation model for water with a water flux that vanishes when the ice-bed gap size goes to zero, the dynamic model not only allows for the process of cavity expansion to be captured dynamically, but also for the dynamic evolution of isolated cavities.

The generalized model in the present paper is in fact formulated in three dimensions. In principle, this avoids another of the

10 limitations of the work in part 1. For practical computational reasons, I have however not been able to run the model in three dimensions, leaving an obvious avenue for future research.

The paper is structured as follows; in section 2.1, I formulate a basic model for viscoelastic ice flow over a rigid bed, with a dynamically-evolving water layer separating ice and bed. The model is reduced using the assumption of small bed slopes in section 2.2, while a numerical method for the reduced model is described in section 2.3. Steady state numerical solutions of

15 the dynamic model are compared with solutions of the simpler viscous steady state model in part 1 in section 3.1. The dynamic approach to steady state is studied in section 3.2, with dynamic cavity connections considered in greater detail in section 3.3. The evolution of overpressurized cavities (in which effective pressure is negative) is described in section 3.4, and the response of isolated cavities to temporal variations in forcing effective pressure is studied in section 3.5. The implication of these results for large scale drainage models and field observations is discussed in section 4.

2 A viscoelastic dynamic model

2.1 The basic model

The model in part 1 is based on the approximation of small bed slopes (Nye, 1969; Kamb, 1970; Fowler, 1981). I will eventually return to that small slope approximation, but first develop a more general three-dimensional formulation. I use a Cartesian

5 coordinate system (x_1, x_2, x_3) with the x_3 axis oriented perpendicularly to the mean glacier bed and x_1 in the mean downslope direction (figure 1), and denote time by t. The rheology of ice is treated here as an elastically compressible upper-convected Maxwell fluid, in which stress σ_{ij} is related to strain rate D_{ij} as

$$\frac{(1+\nu)\delta_{ik}\delta_{jl} - \nu\delta_{ij}\delta_{kl}}{E} \overset{\triangledown}{\sigma}_{kl} + \frac{1}{2\eta}\left(\sigma_{ij} - \frac{1}{3}\sigma_{kk}\delta_{ij}\right) = D_{ij}. \tag{3}$$

where the superscript $\triangledown$ denotes the usual upper-convected derivative

10 $$\overset{\triangledown}{\sigma}_{ij} = \frac{\partial \sigma_{ij}}{\partial t} + u_k \frac{\partial \sigma_{ij}}{\partial x_k} - \frac{\partial u_i}{\partial x_k}\sigma_{kj} - \frac{\partial u_j}{\partial x_k}\sigma_{ik}, \tag{4}$$

where (u_1, u_2, u_3) denotes the velocity field. Strain rate is defined in terms of velocity through

$$D_{ij} = \frac{1}{2}\left(\frac{\partial u_i}{\partial x_j} + \frac{\partial u_j}{\partial x_i}\right). \tag{5}$$

Here, E is Young's modulus, ν is Poisson's ratio and η is viscosity. In response to abrupt changes in stress (with large $\partial \sigma_{kl}/\partial t$, the rheology reduces to

$$\frac{(1+\nu)\delta_{ik}\delta_{jl} - \nu\delta_{ij}\delta_{kl}}{E}\frac{\partial \sigma_{kl}}{\partial t} = D_{ij},$$

as the strain due to the change in stress remains small over such short intervals, and hence the advection terms in the upper-convected derivative are small compared with the time derivative. Integrating over the time interval over which the stress change is imposed, it is then clear that the material behaves temporarily as a linear elastic material subject to a viscous pre-stress. If the change in stress occurs over an interval (t_i, t_f), then with the change in stress related to the corresponding linearized strain as

$$\frac{(1+\nu)\delta_{ik}\delta_{jl} - \nu\delta_{ij}\delta_{kl}}{E}[\sigma_{ij}(x, t_f) - \sigma_{ij}(x, t_i)] = \varepsilon_{ij}(x) = \int_{t_i}^{t_f} D_{ij}(x, t)\mathrm{d}t.$$

Conversely, to emulate Glen's law (Cuffey and Paterson, 2010) over long timescales, when the derivative $\overset{\triangledown}{\sigma}_{kl}$ becomes negligible, one would put $\eta = B|\sigma|^{1-n}/2$ where n and B are the usual exponent and coefficient in Glen's law, and σ is the usual second invariant of the stress tensor,

$$\sigma = \sqrt{\sigma_{ij}\sigma_{ij}/2}.$$

In this paper, I will continue to focus on a simpler version of the model with constant viscosity as in section 3.1.

I assume ice occupies a domain defined by $x_3 > b(x_1, x_2) + h(x_1, x_2, t)$, where b is a fixed bed elevation and $h \geq 0$ is an

15 ice-bed gap thickness that can evolve over time. b here is identical to its meaning in part 1 (as shown in figure 1 therein), while

the sum of bed elevation and gap thickness $b + h$ is the cavity roof elevation h_C in part 1. I assume that the domain represents a boundary layer near the base of the glacier (Fowler, 1981). Consequently, I assume as in part 1 that gravitational body forces contribute negligibly to stress compared with overburden, and conservation of momentum can be written in the form

$$\frac{\partial \sigma_{ij}}{\partial x_j} = 0, \tag{6}$$

5   ignoring inertial effects. Conservation of mass requires

$$\frac{\partial \rho}{\partial t} + \frac{\partial (\rho u_i)}{\partial x_i} = 0. \tag{7}$$

In common with typical models in elasticity, this equation can be used *a posteriori* to compute variations in density due to elastic compression of the material, but is not necessary to compute the velocity field.

At the lower boundary $x_3 = b(x_1, x_2) + h(x_1, x_2, t)$, I assume that there is free slip regardless of whether the macroscopic

10 ice-bed separation h vanishes or not. In the absence of an ice-bed gap in the model, I assume that interfacial premelting (Dash et al., 1995) still generates a microscopic film that ensures ensure negligible shear stress; this is a standard assumption of basal sliding theory. Denoting by n_i the unit normal to the lower boundary of the ice, this implies

$$(\delta_{ij} - n_i n_j) \sigma_{jk} n_k = 0. \tag{8}$$

The lower boundary also satisfies a kinematic boundary condition of the form

15 $$u_3 = \frac{\partial h}{\partial t} + u_1 \frac{\partial (b + h)}{\partial x_1} + u_2 \frac{\partial (h + b)}{\partial x_2}. \tag{9}$$

where melt is taken to be negligible.

To close the problem, I require one additional boundary condition. I consider two alternatives. First, the standard assumption in dynamic models of subglacial cavity formation (Durand et al., 2009; Stubblefield et al., 2021; de Diego et al., 2021) has been that the bed is rigid yet highly permeable, with a prescribed water pressure p_w^0 everywhere. That assumption is also part

20 of the steady state model by Fowler (1986) and Schoof (2005) that I previously generalized in part 1. Normal stress cannot drop below that water pressure, as water forces its way between ice and bed and opens a gap or cavity. A fully permeable bed gives a boundary condition on normal stress in the either-or form

$$-\sigma_{ij} n_i n_j = p_w^0 \qquad \qquad \text{if } h > 0 \text{ or } \left(h = 0 \text{ and } \frac{\partial h}{\partial t} > 0 \right) \tag{10a}$$

$$-\sigma_{ij} n_i n_j \geq p_w^0 \qquad \qquad \text{if } h = \frac{\partial h}{\partial t} = 0, \tag{10b}$$

25 signifying the possibility that compressive normal stress can exceed water pressure where ice is in contact with the bed, and a gap is not about to form: put more simply, in contact areas, normal velocity is prescribed, while in areas with an ice-bed gap, normal stress is prescribed, and the inequality constraints above serve to determine which boundary condition applies where (see also Stubblefield et al., 2021).

The boundary conditions above do not permit the formation of hydraulically isolated cavities, or of underpressurized contact

30 areas that remain hydraulically isolated as in part 1. As an alternative to (10), I therefore consider a bed that is perfectly

impermeable except in specific locations at which water from an ambient drainage system can enter or exit the ice-bed gap. Specifically, I assume that there is a (typically small) permeable portion P of the bed at which (10) holds, while for the remainder, I assume that an active hydraulic system inside the ice-bed gap redistributes water.

Outside of P, I assume that there is a water column of evolving height h_w inside the ice-bed gap, constrained by $0 \leq h_w \leq h$.

5 The water column height satisfies a mass conservation equation of the form

$$\frac{\partial h_w}{\partial t} + \frac{\partial q_1}{\partial x_1} + \frac{\partial q_2}{\partial x_2} = 0. \tag{11a}$$

Anticipating the development in the next section, I assume that the ice-bed gap is shallow and the depth-integrated water flux $\mathbf{q} = (q_1, q_2)$ can be related to water column height h_w and an along-bed gradient in water pressure $p_w(x_1, x_2, t)$ as

$$\mathbf{q} = -K\left(h_w, |\nabla_h p_w|\right) \nabla_h p_w + \frac{1}{2}\mathbf{u}_h h_w \tag{11b}$$

10 where

$$\nabla_h p_w = \left(\frac{\partial p_w}{\partial x_1}, \frac{\partial p_w}{\partial x_2}\right), \tag{11c}$$

$\mathbf{u}_h = (u_1, u_2)$ is the horizontal component of velocity at the base of the ice, and the two-dimensional "gap permeability" K vanishes when h_w does. The first term in the definition of $\mathbf{q}$ describes pressure-gradient-driven Poiseuille-type flow, while the second term represents shear in the water layer, and I crudely treat the two as additive. In practice I will use a Darcy-Weisbach

15 or Manning-Gauckler power law formulation (see e.g. Werder et al., 2013) of the generic form

$$K(h_w, |\nabla_h p_w|) = k_0 h_w^\alpha |\nabla_h p_w|^{-1/2} \tag{11d}$$

with $\alpha > 1$ and $\kappa_0 > 0$ constant. Note also that the *local* water pressure p_w is not identically equal to the imposed drainage system pressure p_w^0 except at the boundaries of the permeable portion P of the bed, and must be solved for as part of the solution elsewhere.

20 The assumption that shear- and pressure-gradient-driven flow are additive is unlikely to be significant, as I assume that the coefficient k_0 is large, and flux $\mathbf{q}$ is generally dominated by the first, pressure-gradient-driven term. In particular, significant water pressure gradients only occur during brief periods of rapid adjustment in the ice-bed gap size, as a result of abrupt changes in forcing effective pressure N, or when cavities connect, or a previously isolated part of the bed becomes flooded. These connections then occur in a manner similar to hydrofracture (Spence et al., 1985; Tsai and Rice, 2010), and involve water

25 moving much faster (due to the high permeability) than the motion of the ice. Shear in the water column therefore remains a negligible contribution to water flux.

At all other times, with a large gap permeability, the water flux required to account for more gradual changes in the ice-bed gap can be generated by small pressure gradients. In other words, the flux relation (11b) then simply serves at leading order to impose a constant water pressure in each basal cavity. In that case, too, shear in the water column plays an insignificant

30 role, and the second term $\mathbf{u}_h h_w/2$ in the definition of flux is retained here formally simply to make the switch to a moving

coordinate frame employed in section 2.3 more self-consistent (since an advective term will automatically appear under the change to a moving frame).

Key to the model is that the gap permeability K goes to zero when h_w does, allowing cavities to become disconnected from each other when they are separated by parts of the bed on which $h = h_w = 0$, or where h is close to zero. This allows isolated cavities to form, where a fixed volume of water becomes trapped in a part of the bed with no access to the permeable region P. A vanishing gap permeability at vanishing h_w also ensures that water cannot spuriously be removed from parts of the bed that contain no water, so $h_w \geq 0$.

Importantly, the stipulation that $K = 0$ when $h_w = 0$ allows (11a) to be used across the whole bed except the permeable region P (where water pressure p_w is fixed and water mass can be supplied or removed through the permeable bed, implying that a source term that is omitted in (11a)). This is the case regardless of whether any water is present or indeed, whether there is a non-zero ice-bed gap or not. In that vein, note also that the mass conservation equation (11a) should be understood in weak form, thus potentially permitting mass-conserving shocks in h_w.

I continue to identify p_w with the compressive normal stress at the bed

$$-\sigma_{ij} n_i n_j = p_w \tag{11e}$$

even if no water is present. As discussed above, there is also no water flux in that case despite the possibility of a non-zero gradient in p_w, since $K = 0$ when $h_w = 0$.

Equation (11e) would close the model if one could also identify h_w with the gap width. Here I account at least formally for the possibility that water pressure can drop to zero (or more precisely, to the triple point pressure, which I take to be low enough to be indistinguishable from zero), so a vapour-filled gap between water and ice can form. In that case, $h_w < h$ and the evolution of the ice-bed gap h is not given locally by (11a). A similar approach is taken to water flow in partially filled cavities in the large scale drainage model of Schoof et al. (2012).

Worrying about vapour-filled gaps may seem excessive given the typically large overburden and water pressures involved. However, purely elastic hydrofracture problems similar to the one studied here predict negative fluid pressure singularities at the contact lines of cavities unless a "fluid lag" in the form of a gas-filled region near the tip of the crack is included in the model formulation (Spence et al., 1985; Tsai and Rice, 2010, 2012). Consequently, I adopt the slightly more complicated formulation

$$h_w = h \qquad\qquad \text{if } p_w > 0, \tag{11f}$$
$$h_w \leq h \qquad\qquad \text{if } p_w = 0, \tag{11g}$$

and p_w cannot be negative. Note that the conditions (11f)–(11g) also capture the physics ice-bed contact areas on which $h = 0$. If there is no access to the ambient drainage system, contact will be maintained if $p_w > 0$, meaning (despite the misleading notation) that compressive normal stress is positive (since $p_w = -\sigma_{ij} n_i n_j$ everywhere). Conversely, when compressive normal stress vanishes, the constraint $h \geq h_w \geq 0$ implies that h cannot decrease below zero, and hence (11g) implies that $\partial h/\partial t \geq 0$ if $h = 0$ and $p_w = 0$. This is the analogue of (10) for a contact area on an impermeable part of the bed.

As far field boundary conditions, I consider prescribed normal and shear stress, in the form

$$-\sigma_{33} \to p_i, \qquad \sigma_{13} \to \tau_b, \qquad \sigma_{23} \to 0 \tag{12}$$

as $x_3 \to \infty$, where p_i is overburden and τ_b is the usual 'basal shear stress' of the theory of basal sliding (Fowler, 1981). In addition, I assume the domain is laterally periodic, with period a in both horizontal directions.

2.2 Shallow bed topography

Significant simplifications can be obtained by considering flow over 'shallow' bed roughness, meaning, a bed $b(x_1, x_2)$ with small slopes (see e.g. Nye, 1969; Kamb, 1970; Fowler, 1986; Schoof, 2005). To obtain a simplified model systematically, I sketch the required non-dimensionalization here, building primarily on the seminal work of Fowler (1981). Define a horizontal length scale $[x]$ for typical bed roughness wavelengths, and a scale $[b]$ for the amplitude of roughness. This leads to a slope scale

$$\nu = \frac{[b]}{[x]},$$

and the basis of the approximations that follow will be $\nu \ll 1$. With a sliding velocity scale u_b for motion parallel to the bed, I can define a scale for velocity variations induced by deformation around bed topography as $[u] = \nu u_b$, and a corresponding (viscous) stress scale as $[\sigma] = \eta[u]/[x]$. A natural choice of time scale is the advective $[t] = [x]/u_b$, and I assume that there is a density scale $[\rho]$ given by the density of ice subject to zero stress.

With these scales in hand, I can define dimensionless variables as

$$(x_1, x_2, x_3) = [x](x_1^*, x_2^*, x_3^*), \qquad (u_1, u_2, u_3) = u_b(\bar{u}, \bar{v}, 0) + [u](u_1^*, u_2^*, u_3^*),$$

$$p_w = p_i + [\sigma]p_w^*, \qquad \sigma_{ij} = \begin{cases} -p_i + [\sigma]\sigma_{33}^* & \text{if } i = j = 3, \\ [\sigma]\sigma_{ij}^* & \text{otherwise,} \end{cases} \qquad \rho = [\rho]\rho^*$$

$$b = [b]b^*, \qquad h = [b]h^*, \qquad h_w = [h]h_w^*.$$

In addition, I obtain the following dimensionless parameters

$$\tau_M = \frac{2\eta}{E[t]}, \qquad \kappa = \frac{[t]K([b], [\sigma]/[x])[\sigma]}{[b][x]^2} = \frac{k_0[t][b]^{\alpha-1}[\sigma]^{1/2}}{[x]^{3/2}}, \qquad \tau_b^* = \frac{\tau_b}{\nu[\sigma]}, \qquad N^* = \frac{p_i - p_w^0}{[\sigma]}. \qquad p_i^* = \frac{p_i}{[\sigma]}$$

Here τ_M is a dimensionless Maxwell time, κ is a dimensionless ice-bed gap permeability and τ_b^* is a dimensionless basal shear stress. N^* is the (scaled) usual effective pressure defined as the difference between overburden and the water pressure in the 'ambient' drainage system to which the bed is connected in the permeable regions P, while p_w^* is a reduced water pressure, defined as the difference between local water pressure and overburden: p_w^* is in the negative of the effective pressure define in terms of *local* rather than forcing water pressure.

Going forward, I will assume that $\nu \ll 1$. In addition, the Maxwell time $\tau_M \ll 1$ is short (so that the ice for the most part behaves as a viscous material, as is the case in existing models for subglacial cavity formation) and permeability $\kappa \gg 1$ is large (so that water pressure in a connected portion of the ice-bed gap rapidly equalizes, as is also assumed in existing models, which

do not attempt to model the dynamic redistribution of water inside cavities). However, unlike ν, both τ_M and κ will be retained explicitly in the model to capture rapid changes in ice-bed gap during cavity connection events.

I omit the asterisk decorations immediately for improved readability. To an error of $O(\nu)$, the model becomes

$$\tau_M \left[(1-\nu)\delta_{ik}\delta_{jl} - \nu\delta_{ij}\delta_{kl} \right] \left(\frac{\partial \sigma_{kl}}{\partial t} + \bar{u}\frac{\partial \sigma_{kl}}{\partial x_1} + \bar{v}\frac{\partial \sigma_{kl}}{\partial x_2} \right) + \sigma_{ij} = \frac{\partial u_i}{\partial x_j} + \frac{\partial u_j}{\partial x_i} \qquad \text{for } x_3 > 0, \tag{13a}$$

$$\frac{\partial \rho}{\partial t} + \bar{u}\frac{\partial \rho}{\partial x_1} + \bar{v}\frac{\partial \rho}{\partial x_2} = 0 \qquad \text{for } x_3 > 0, \tag{13b}$$

$$\frac{\partial \sigma_{ij}}{\partial x_j} = 0 \qquad \text{for } x_3 > 0 \tag{13c}$$

$$\sigma_{i3} = 0 \qquad \text{for } i = 1, 2 \text{ at } x_3 = 0 \tag{13d}$$

$$\sigma_{33} = -p_w \qquad \text{at } x_3 = 0 \tag{13e}$$

$$\frac{\partial h}{\partial t} + u_1 \frac{\partial(b+h)}{\partial x_1} + u_2 \frac{\partial(h+b)}{\partial x_2} = u_3 \qquad \text{at } x_3 = 0 \tag{13f}$$

$$\tag{13g}$$

with two possible closures. The first, which I refer to as a permeable bed, puts

$$-\sigma_{33} = N \qquad \text{if } h > 0 \text{ or } \left(h = 0 \text{ and } \frac{\partial h}{\partial t} > 0 \right) \tag{14a}$$

$$-\sigma_{33} \geq N \qquad \text{if } h = \frac{\partial h}{\partial t} = 0 \tag{14b}$$

at $x_3 = 0$. The second, which I refer to as an impermeable bed, imposes the boundary conditions (14) only when $(x_1, x_2) \in P$ is in a part of the bed to which the ambient drainage system has access, and flow of water occurs only through the ice-bed gap otherwise, satisfying

$$\frac{\partial h_w}{\partial t} + \nabla_h \cdot \mathbf{q} = 0, \tag{15a}$$

$$\mathbf{q} = -\kappa h_w^{\alpha} |\nabla_h p_w|^{-1/2} \nabla_h p_w + \frac{1}{2} h_w \bar{\mathbf{u}} \tag{15b}$$

$$h_w = h \qquad \text{if } p_w > -p_i, \tag{15c}$$

$$h_w \leq h \qquad \text{if } p_w = -p_i. \tag{15d}$$

with $p_w \geq -p_i$, and $\bar{\mathbf{u}} = (\bar{u}, \bar{v})$. The far field boundary conditions are

$$\sigma_{i3} \to 0 \qquad \text{for } i = 1, 2, 3 \text{ as } x_3 \to \infty. \tag{16}$$

As in other models of basal sliding with small-slope bed roughness (Nye, 1969; Kamb, 1970; Fowler, 1981, 1986; Schoof, 2005), the basal shear stress τ_b^* is a higher order correction to the basal stress field: a relationship between the applied shear stess $(\tau_b, 0)$ and the sliding velocity $(\bar{u}, \bar{v})$ (that is, a friction law) can be computed by considering overall force balance at first order in ν. Doing so leads to the following integral constraints (Fowler, 1981)

$$\tau_b = -\frac{1}{a^2} \int_0^a \int_0^a \sigma_{33} \frac{\partial(h+b)}{\partial x_1} \mathrm{d}y\mathrm{d}x, \qquad 0 = \frac{1}{a^2} \int_0^a \int_0^a \sigma_{33} \frac{\partial(h+b)}{\partial x_2} \mathrm{d}y\mathrm{d}x, \tag{17}$$

where a is the scaled period of the bed. While this is the main objective of many treatments of basal cavitation, my main goal here is to understand the evolution of basal connectivity instead, and I forego the computation of basal drag as a function of sliding velocity, simply imposing a constant sliding velocity: to that end, I also assume that sliding only occurs in x_1-direction, and put $\bar{v} = 0$.

5   At first sight, this may not seem all that different from the original model of section 2.1. From a computational perspective, major advantages of the reduced model arise from the linearization of the upper-convective derivative into a much simplified material derivative in (13a): effectively, the effect of the small slope approximation alone is similar to the usual small-strain approximation that can be obtained when explicitly taking the limit of a small Maxwell time. In addition, the small slope approximation reduces the free boundary problem for the lower boundary of the ice into a problem posed on a fixed domain 10 $x_3 > 0$, in which the type of boundary condition that applies at any given part of the boundary must be determined as part of the solution through the inequality constraints in the boundary conditions (14) or (15).

2.3   Numerical method

Computationally, the problem defined in the previous section is well-suited to solution by mixed finite elements in order to handle both, the viscoelastic rheology and the inequality-constrained boundary conditions as described in Stubblefield et al. 15 (2021) and de Diego et al. (2021, 2022). Unlike these previous studies, an in-depth analysis of the numerical algorithm is not my goal here, in large part due to the complications introduced by the dynamic drainage model (15a). Instead, I hope to spur interest in the problem and development of more sophisticated approaches by showing results using the simplest approach that appears capable of discretizing and solving the model as stated.

    I use a coordinate frame moving at the sliding velocity $(\bar{u}, 0)$ to eliminate the advection terms in (13a) and (13f), and use a 20 backward Euler step to semi-discretize in time. At each time step, (13a) combined with (13c) then takes the mathematical form of a compressible linear elasticity problem, with velocity taking the place of displacement, and "elastic" moduli that differ from E and ν, and depend on step size δt. Instead of applying the far field boundary conditions (16) at infinity, I apply them at a finite distance D from the bed to ensure a finite domain size. I solve (13a) with (13c)–(13e) in weak form, using piecewise linear finite elements to discretize the velocity field, piecewise constant elements for stress, with a piecewise linear representation 25 along boundary elements for p_w and h. Although piecewise linear finite elements are appropriate for compressible elastic problems of the type solved at each time step (Kikuchi and Oden, 1988), a more sophisticated choice of basis functions may in fact be preferable here as the long time scale behaviour of the solution can be expected to mimic an incompressible viscous fluid (e.g. Arnold et al., 1984).

    To handle the mass conservation problem (15a), I use a finite volume discretization with piecewise constant h_w, approxi-30 mating gradients in p_w on element boundaries by using the same piecewise linear representation of p_w as in the weak form of (13e). A finite volume scheme is mass conserving by construction, which is essential in modelling isolated cavities. I use an upwind scheme for K to prevent water depth h_w becoming spuriously negative where there is net water drainage out of a cell. Doing so requires an upwind direction to be defined. I use the upwind direction defined by the water pressure gradient solved for in the previous time step.

Note that in similar elastic problems solved elsewhere, water can never be removed completely from a pre-existing gap, though it can become arbitrarily thin (Touvet et al., 2011; Warburton et al., 2020). The distinction between a very thin gap and no gap at all is of little consequence here, since I assume that there is free slip at the base of the ice regardless of whether $h_w > 0$, and the permeability approaches zero as h_w does.

5   The use of piecewise constant finite volumes for h_w conflicts with the natural discretization of h using piecewise linear finite elements; I handle this by using a finite volume mesh based on a Voronoi tessellation of the bed that is dual to the Delaney triangulation used for the finite element mesh, ensuring that nodes on which h and p_w are evaluated as part of the finite element discretization are also cell centres on which h_w are defined. I then impose the conditions (15d) and (15c) pointwise at these nodes / cell centres.

All inequality constraints that are part of the boundary conditions for either the impermeable or permeable bed case can be written as complementarity problems in discretized form, of the generic form

$$f(y_1) \geq 0, \qquad g(y_2) \geq 0, \qquad f(y_1)g(y_2) = 0;$$

take (15c)–(15d) as an example, where $y_1 = h - h_w$, $y_2 = p_w + p_i$ and $f(y_1) = y_1$, $g(y_2) = y_2$. I reformulate each of these complementarity problems generically in the semi-smooth form (see also de Diego et al., 2021, 2022; Zarrinderakht et al., 2022)

$$\min(f(y_1), g(y_2)) = 0,$$

10   and use a semi-smooth Newton method to solve for each backward Euler step.

The code is written in MATLAB and uses neither adaptive time stepping (beyond automatic step size reduction when the Newton solver fails to converge to a prescribed tolerance for a given backward Euler step) nor adaptive meshing (although the mesh used is non-uniform, with nodes concentrated near the bed). Both of these features would be desirable future improvements. Although the code is implemented for both, two- and three-dimensional domains, the lack of adaptive meshing still

15   leads to a relatively coarse resolution along the bed, and restricts any realistic use of the code to two dimensions.

3   Results

In the numerical results reported here, I use the model (13) with a prescribed sliding velocity $\bar{u} = 1$, $\bar{v} = 0$ in a two-dimensional domain of width $a = 2\pi$, and I employ the simper notation $(x, z) = (x_1, x_3)$. I use plane strain conditions, in which $u_2 = 0$ and none of the variables depend on x_2, but transverse normal stress σ_{22} is generally not zero or constant in time. I use the

20   double-humped bed defined by

$$b(x) = \sin(x) + \sin(2x) \qquad (18)$$

which is identical to equation (10) of part 1 with $h_0 = 1$, $a = 2\pi$. In addition, I either assume a fully permeable bed so that the constraints (14) hold, or I assume that only part of the bed is permeable, applying (14) on a subset P of the bed. In that , I set P to be either a small interval around $x_P = 1.64$, or a small interval around $x_P = 4.65$, while (15) holds across the remainder

of the bed. The locations x_P are chosen to be identical to those used in part 1, and correspond to the locations where cavities form at the lowest possible effective pressures N.

I use a finite domain depth $D = a$, and the finite element mesh consists of 9419 triangles with 4811 non-uniformly distributed nodes, of which 178 are at the bed and form the cell centres of the finite volume tessellation of the bed. This degree of resolution

5 was practically the maximum I could achieve in MATLAB, multi-threading on six to eight processors. I use a short Maxwell time $\tau_M = 1/50$ and large permeability $\kappa = 70$, with the intention of representing a viscous limit for the ice and inviscid behaviour in the water column at $O(1)$ time scales. The dimensionless overburden is set to $p_i = 10^3$, and in practice (at the resolution that I am able to achieve), the condition (15d) for generating a partially vapour-filled ice-bed gap was never satisfied in the discretized model.

For the purpose of visualizing results, I focus mostly on several easy-to-identify scalar attributes of the solution and their evolution in time, plotting only selected cavity profiles. I identify cavity end points b_j and c_j as the end points of any finite intervals above a minimum threshold size of $|c_j - b_j| \geq 0.15$, in which gap width h exceeds $h_\epsilon = 5 \times 10^{-4}$) everywhere. As measures of cavity size that are commonly used in large scale subglacial drainage models (the scale of individual cavities being "microscopic" in these models, see Hewitt, 2011; Schoof et al., 2012; Werder et al., 2013), I compute a mean cavity size $\bar{h}$ and cavitation ratio θ (Thøgersen et al., 2019) defined by

$$\bar{h}(t) = \frac{1}{a} \int_0^a h(x,t)\mathrm{d}x, \qquad \theta(t) = \frac{1}{a} \int_0^a H(h(x,t) - h_\epsilon)\mathrm{d}x$$

10 where H is the usual Heaviside function. Note that θ is simply the fraction of the bed that is cavitated, since $\theta = a^{-1} \sum (c_j - b_j)$, the sum being taken over all cavities in one bed period.

3.1 Steady states: a test case

The dynamic model of section 2 should agree with the simpler, purely viscous model of part 1 in the limit of a short Maxwell time τ_M (thus ensuring an absence of elastic effects) and of a large cavity permeability parameter κ (ensuring negligible water

15 pressure gradients except where water layer depth h_w vanishes, or nearly does), provided the solution is also in steady state. To test the numerical solution of the dynamic model, I therefore compare its steady state results with the results of the model of part 1 for the same forcing effective pressure N, and for the same isolated cavity volumes when these are present (figure 2). Note that the problem in part 1 is solved by an entirely different numerical method from that in section 2.3, providing a robust test.

20 There is an important qualification to the meaning of "steady state" here: I simply compute a numerical solution of the model (13), subject to (14) in P and (15) elsewhere, for a long time interval. The numerical method in section 2.3 employs a moving frame, so a steady state solution of the underlying dynamic model is a travelling wave solution in that moving frame. In practice, the solution retains residual oscillations even for large times t. Provided the contact area is substantially larger than a few finite volume cells, these residual oscillations are small (figure 3), and I interpret them as numerical artifacts resulting from
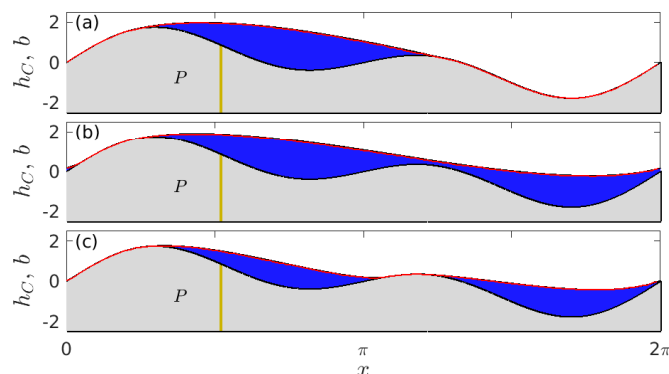
Figure 2. Comparison of steady cavity roof geometry (denoted by $b + h$ for the dynamic model, h_C for the steady viscous model of part 1) for $x_P = 1.64$. The bed b is shown in grey, with the permeable bed portion P in beige. The result for the dynamic model is shown as a blue shaded cavity, the result of the steady state model of part 1 as a red curve. a) $N = 1.053$ before cavity expansion, b) $N = 1.053$ after cavity expansion and c) $N = 2.37$, with an isolated cavity volume of $V_2 = 1.87$ imposed in the model of part 1, the volume having been computed from the dynamic solution. Note that this cavity volume is different from the value of $V_2 = 1.062$ for the isolated cavities that form under quasi-steady conditions for the same bed in part 1. The two cavity roof shapes are practically indistinguishable in each case.

the use of a travelling coordinate frame, combined with the inherent heterogeneity involved in an unstructured mesh (which is also still relatively coarse, with 178 finite volume cells at the lower domain boundary).

The solutions of the dynamic model plotted in figure 2 are therefore not strictly numerical steady states, but an effectively random instant within that residual oscillation cycle. That said, figure 2 shows close agreement between the solution of the

5 dynamic model and the steady state solution of part 1, at least for the moderate values of N for which the dynamic model produces a recognizable near-steady state within a reasonable time span. This applies equally for solutions with and without isolated cavities. Note however that the isolated cavity volume in figure 2c differs from that predicted in section 3 of part 1. That is unsurprising: the isolated cavity volume computed there by the viscous steady state model of part 1 results from a very slow change in N and a cavity configuration that is at all times in a quasi-steady state. To compute the solution in figure 2,

10 I use instead an abrupt, finite jump in N to force changes in cavity configuration (see also figure 3). At the instant when a cavity becomes isolated, the latter is generally not in steady state, or at the critical value of N at which steady state cavities first become isolated, and consequently we cannot expect isolated cavity volume to be the same as that computed in part 1.

3.2 Dynamic approach to equilibrium

The purpose of introducing a dynamic model is precisely to study the transient behaviour leading up to the eventual steady state.

15 Figure 3 shows time series of forcing effective pressure N, cavity end positions b_j and c_j, mean cavity size $\bar{h}$ and cavitation ratio θ as the bed is forced with step changes in N through a permeable patch at $x_P = 1.64$.

As expected from part 1, the steady state mean water depth $\bar{h}$ and cavitation ratio θ increase as N is decreased, and the rapid expansion of the cavity after $t = 78$ is irreversible. The dominant feature of the time series is however the overshoot in $\bar{h}$ after
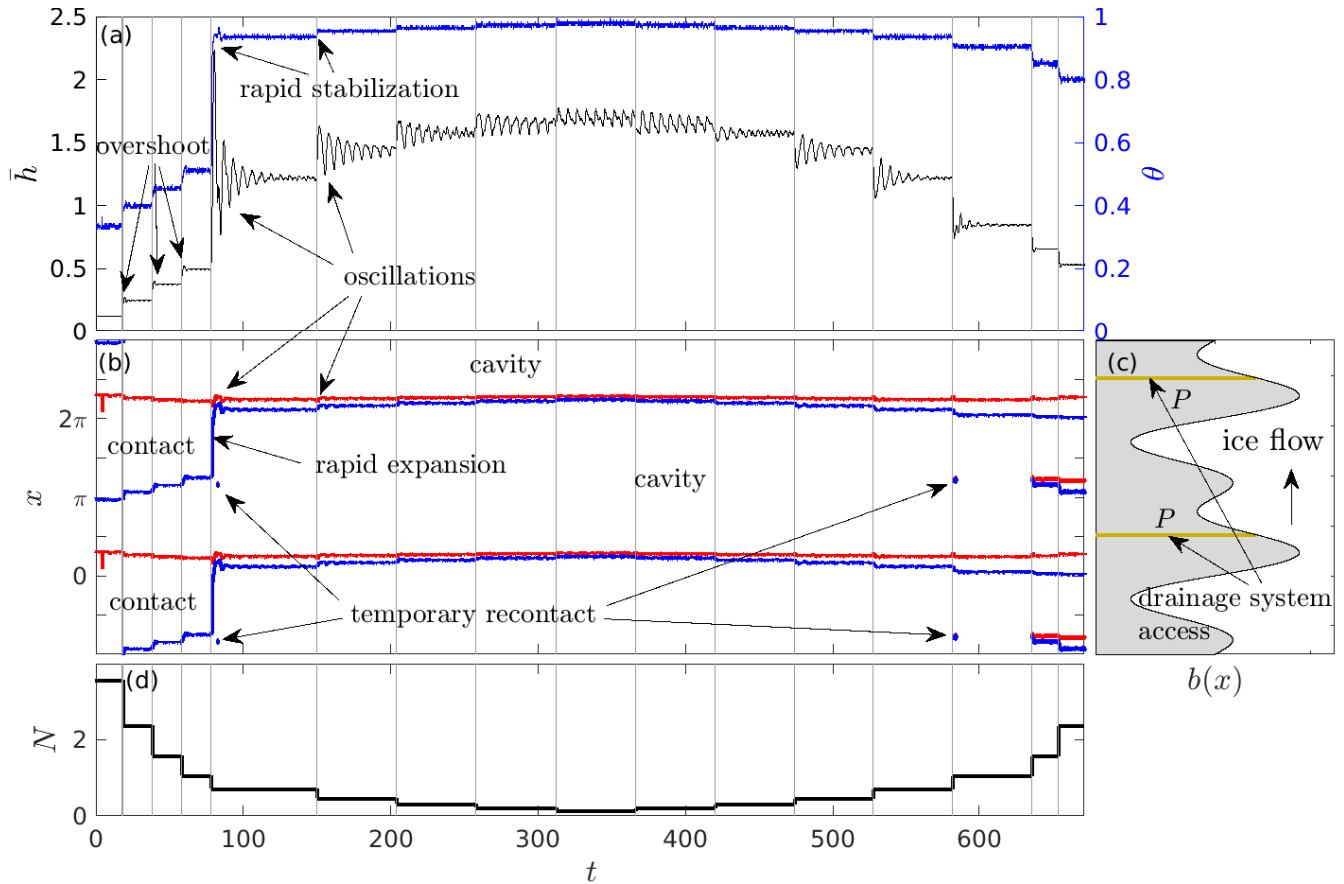
Figure 3. Dynamic cavity evolution under step changes in forcing effetive pressure N with $P = \{1.64\}$. (a) Mean cavity depth $\bar{h}$ (black, left-hand axis) and cavitation ratio θ (blue, right-hand axis) against time t. (b) Cavity end point locations at the upstream (red) and downstream (blue) end of cavities against t. (c) The corresponding shape of the bed with permeable region P in beige. The direction of ice flow (in the positive x-direction) is indicated by an arrow; the flipped x and b axes mean that the bed shape is a mirror image of that in figure 2. (d) The forcing effective pressure N as a function of time. Grey vertical lines in panels (a)–(b) and (d) indicate abrupt changes in N. The solutions in panels (a)–(c) of figure 2 correspond to the solutions here at $t = 78$, $t = 636$ and $t = 670$, respectively

each step in N occurs: $\bar{h}$ transiently exceeds its new equilibrium value following each decrease in N, and conversely drops below its equilibrium value following an increase in N. This overshoot is barely perceptible at the scale shown in figure 3 for cases where a significant part of the bed remains uncavitated (with θ close to 0.5, at times prior to $t = 78$), or when there are two separate contact areas (after $t = 636$). The overshoot is much more clearly visible for the latter case in the solutions shown

5   in figure 4, where a shorter overall time interval is plotted.

The overshoot becomes large once there is only a single contact area with a cavitation ratio close to unity (between $t = 78$ and $t = 636$ in figure 3). In each case, the overshoot is followed by an oscillatory approach to equilibrium. Once again, the nature of the oscillatory approach to equilibrium depends on the extent of cavitation: when there is a single contact area with θ close to unity, the dominant (peak-to-peak) period of oscillation is close to the advective time scale $a/\bar{u}$ for one bed wavelength

10   a, and attenuation to equilibrium is slow, often taking several oscillation periods for the amplitude to halve. The magnitude of the overshoot and subsequent oscillations is largest immediately after contact with the smaller bed protrusion is lost and the cavity expands rapidly after $t = 78$: in fact, the oscillations are large enough for the ice to contact the smaller bed protrusion temporarily as marked in figure 3(b).

Conversely, if there is limited cavity extent with only the lee of the larger bed protrusion cavitated and θ close to 0.5 (again

15   prior to $t = 78$), or if there are two separate contact areas (after $t = 636$) attenuation is much more rapid, and the dominant peak-to-peak period is approximately half the advection time scale for one bed wavelength. Additional bed contact therefore appears to have a significant damping effect on the oscillations.

The most sustained oscillations occur when there is a single, small contact area in each bed period (an arguably contrived situation for real glacier beds). Note that the cavitation ratio θ overshoots only slightly (figure 3(a)), and approaches equilibrium

20   rapidly while cavity height $\bar{h}$ continues to oscillate significantly. Cavitation ratio and ice-bed gap size are therefore not good proxies for each other. Closer inspection of the cavity end point locations in figure 3(b) for the interval between $t = 78$ and $t = 636$ indicates that the continued oscillations in $\bar{h}$ coincide with in-phase oscillations of both cavity end points. In the absence of comparable oscillations in θ, this implies a back-and-forth motion of the contact area, without significant change in its size. That contact area motions occurs around the top of the prominent bed protrusion at $x = 0.8$. A change in position of the

25   contact area there leads to a significant fractional change in the slope $\partial b/\partial x$ that the ice is incident on (since this location is the maximum of b, where $\partial^2 b/\partial x^2$ is large and negative). Changes in bed slope in the contact area in turn affect normal velocities through (13f) (where the ice-bed gap h vanishes in the contact area). These variations in normal velocity are presumably the reason for the significant oscillations in $\bar{h}$.

Repetition of an earlier note of caution in interpreting these results is however in order here: for the lowest effective pressures

30   N in figure 3 (between $t = 258$ and $t = 420$), the oscillation in $\bar{h}$ barely attenuate at all, and it is unclear to what extent a steady state is approached. The cavitation ratio is very close to unity here (typically around 0.96–0..97). With such a small contact area, only about 5–7 nodes in the finite element mesh are in contact with the bed, raising the spectre of significant numerical artifacts. Note also that the numerical method treats a bed cell as either separated from the bed with $h > 0$, or in contact with $h = 0$, and the cavity end point location therefore jumps in increments of a single cell size, giving the plots of θ and of cavity

35   end point location against t a non-smooth appearance, while the mean ice-bed separation $\bar{h}$ is much smoother.
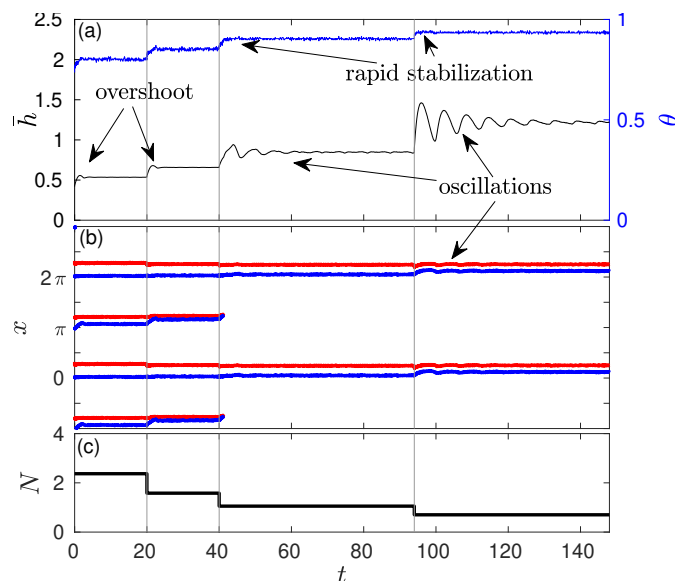
Figure 4. Using the same plotting scheme as in figure 3, dynamic cavity evolution under step changes in N with $P = \{1.64\}$. Here the intial state includes an isolated cavity around $x = 4.65$.

The generic behaviour shown in figure 3 is not unique to either starting with a small cavity and an isolated low-pressure bed region (as is the case before the cavity rapidly expands at $t = 78$), or indeed to having only a limited permeable bed patch P. Figure 4 shows a solution for step changes in N with the same bed configuration as in figure 3, but with an initial condition that includes an isolated cavity in the lee of the smaller bed protrusion. The oscillatory approach to equilibrium clearly mimics that

5   in figure 3, except for the absence of dramatic oscillations following cavity connection (after $t = 78$ in figure 3 and after $t = 40$ here): connection with an existing cavity involves relatively small changes in $\bar{h}$ in figure 4 so the lack of a large overshoot in figure 4 is not surprising.

Figure 5 shows a similar solution for stepwise changes in N, but now with a fully permeable bed. Except for the assumption of a viscoelastic rheology and of small bed slopes, this case is analogous to those in Gagliardini et al. (2007), Helanow et al.

10   (2020, 2021), Stubblefield et al. (2021) and de Diego et al. (2021, 2022). Note that viscoleasticity should be mostly irrelevant here, since there are limited changes in the solution that occur over short time scales $\sim \tau_M$, and where significant changes occur that rapidly, they invariably do so immediately after a step change in N. Here, too, we see that $\bar{h}$ overshoots its equilibrium value and decays in an oscillatory manner, though I have not chosen to run each step in N for long enough to see a complete approach to equilibrium. As in the case of an only partially permeable bed, the oscillations in $\bar{h}$ are again much longer-lasting

15   when there is a single contact area per bed wavelength a, and the period of oscillations approximately doubles when contact is lost with the smaller bed protrusion, while the cavitation ratio does not exhibit the same degree of oscillatory behaviour.
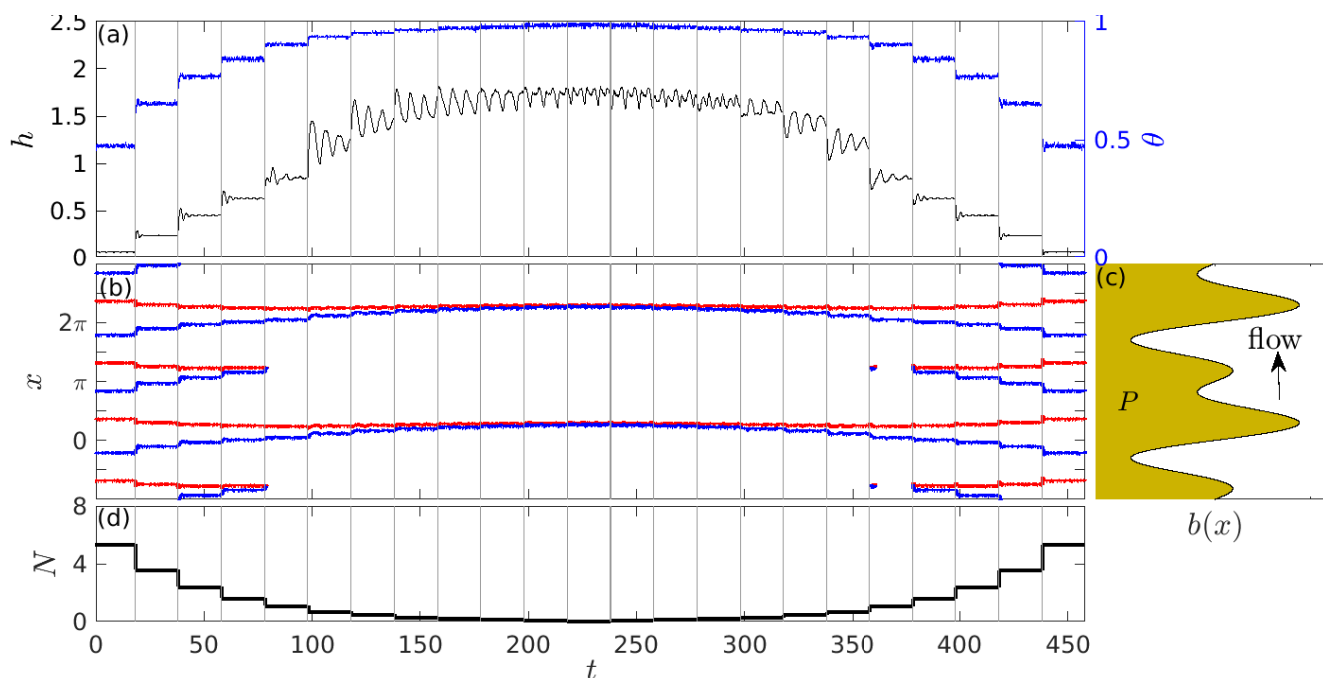
Figure 5. Using the same plotting scheme as in figure 3, dynamic cavity evolution under step changes in N with a fully permeable bed, $P = (0, a)$.

3.3 Dynamic cavity connection

The rather long time interval over which the solution in figure 3 is plotted makes it impossible to see the fine detail of ice-bed gap evolution when a cavity expands rapidly across the top of a bed protrusion, as happens shortly after $t = 78$. Such rapid expansion corresponds to an isolated part of the bed becoming connected to the subglacial drainage system, and is therefore of

5 particular interest.

In figure 6, I focus on that rapid expansion (moving the time origin to the instant that N undergoes the step change that leads to cavity expansion). Prior to expansion, the cavity is in a quasi-steady state (see section 3.1 and figure 2(a)) at $N = 1.05$. In addition to replotting the solution in figure 3, corresponding to a step down to $N = 0.70$, I also compute the response to larger step changes, in order to determine how step size affects the speed and nature of the cavity expansion.

10 Immediately after the drop in N, $\bar{h}$ and θ undergo a rapid but small increase. The increase in cavity size is larger when N drops to a lower value, and is the result of elastic uplift of the ice around the edge of the pre-existing cavity. The speed of the initial expansion is much faster than the advective speed $\bar{u}$, and is presumably controlled by the gap permeability κ as is the case in hydrofracture problems with negligible fracture toughness (Mitchell et al., 2006). I have however not checked for the effect of κ numerically.
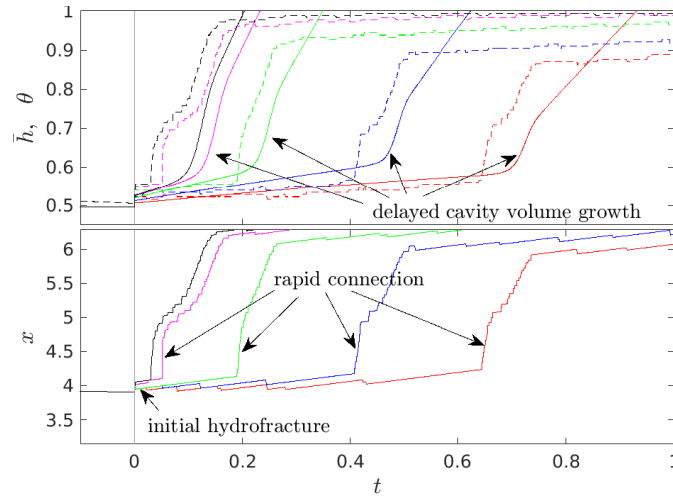
Figure 6. Cavity connection under different step changes in N. The cavity is initially in a (quasi-)steady state with $N = 1.05$ and a single small cavity attached to the larger bed protrusion in the bed 18. N is then changed abruptly at $t = 0$ to values 0.70 (red), 0.47 (blue), 0.21 (green), 0.041 (magenta) 1.6×10^{-3} (black). (a) Cavitation ratio θ (dashed) and mean cavity depth $\bar{h}$ (solid) against time t. (b) Downstream cavity end point position against time t.

Importantly, this initial "hydrofracture" (which is not hydrofracture in the true sense, as it corresponds to a pre-existing fracture being re-opened) has very limited extent, and in fact occurs every time that N goes through a step change, regardless of whether the cavity expands significantly afterwards. The initial rapid increase in cavity size is followed by a period of much more moderate cavity growth, with gradual growth in $\bar{h}$ and the downstream cavity endpoint advancing at speeds comparable

5   to $\bar{u}$ or less. The rate of cavity growth is again greater for lower N.

In interpreting the results for θ and cavity end point position in figure 6, recall that the numerical method uses a travelling frame that moves precisely at speed $\bar{u}$, and cavity end points are by construction located at the finite volume cell centres in that travelling frame. This once more explains the non-smooth appearance of the plots in figure 6(b), and why cavity end points can appear to move backwards, especially for larger values of N (the blue and red curves). That backward motion corresponds to

10   one of the advected finite volume cells going from ice-bed separation to contact. Where such backward motion of the cavity end point does not occur, the cell centre that is the cavity end point moves precisely at $\bar{u}$. Consequently, the relatively coarse spatial resolution limits the ability to resolve variations in the speed of the cavity end point.

The second phase of slower cavity growth is the result of viscous deformation. Only once the downstream cavity end point has advanced significantly downstream does the rapid expansion (or connection) of the cavity past the smaller bed protrusion

15   occur, marked as "rapid connection" in figure 6(b). The precise location of the downstream cavity end point at which this occurs depends slightly on the value of N, with the a less-advanced cavity end point at the onset of cavity connection if N is lower ($c = 4.08$ at $N = 1.6 \times 10^{-3}$ versus $c = 4.23$ at $N = 0.70$). The cavitation ratio is relatively uniform at $\theta \approx 0.56$ for all forcing effective pressures at the onset of connection.

The rapid expansion of the cavity can be separated into two parts: an initial advance of the cavity end point from $c \approx 4.1$ to $c \approx 4.5$ over a time interval around 10^{-2}, somewhat shorter than a single Maxwell time. This is effectively another example of hydrofracture, and is not accompanied by any noticeable change in $\bar{h}$. Subsequently, cavity expansion continues more slowly to a final position around $x \approx 6$, though the cavity end point continues to migrate at speeds greater than $\bar{u}$ during htis phase.

5 It is only during this slower expansion that the cavity depth $\bar{h}$ increases more rapidly. That increase in depth continues after the cavity end point stops advancing rapidly, and eventually leads to overshoot of the equilibrium depth and the oscillations in figure 3(a).

Figure 7 illustrates the evolution of cavity shape for the case of a drop in N to 0.47. The initial condition is shown in panel (a), and the aftermath of the initial hydrofracture in panel (b). The difference between the two is all but imperceptible.

10 Cavity shape immediately before the rapid expansion is shown in panel (c), with the cavity end point having migrated a short but noticeable distance to the top of the smaller bed protrusion. The subsequent rapid expansion of the cavity leads to an extended, thin ice-bed gap extending downstream of the pre-existing cavity (panel d): this corresponds to the rapid increase in θ accompanied by an insignificant change in $\bar{h}$. The gap then thickens more slowly (panel e), leading oscillatory behaviour (panels f–h; these later times are not shown in figure 6). The final steady state is shown in panel (k).

15 ### 3.4 Overpressured cavties

In the computations above, I have focused on a permeable bed section P immediately in the lee of the largest bed protrusion. As explored in part 1, the location of the permeable bed section has major qualitative implications for steady state results. These are replicated in the dynamic model. Figure 8 shows results analogous to figure 3, but with P centered on the downstream side of the smaller bed protrusion, at $x_P = 4.64$.

20 Two solutions are plotted, both of them identical up to $t = 260$. One is forced by N being reduced to close to zero and then increasing again. The other is indicated as "overpressure solution" by arrows and has N lowered successively to $-.46$ and $-.96$. In line with the results in section part 1, we see relaxation to steady states for all positive N, as well as at $N = -.46$, which lies above the critical value $N_{drown} = -0.79$ in figure 5 of part 1. In fact, with a substantial uncavitated portion of the bed, relaxation to steady state is relatively rapid with limited overshoot of cavity size $\bar{h}$ as is also the case for $t < 78$ in figure 3.

25 Only for the lowest value of $N = -.96$ used does complete detachment of ice from the bed occur, with θ reaching unity (figure 8(a)).

3.5 Pressure in isolated cavities

In part 1, I showed that steady-state effective pressure in isolated cavities is remarkably insensitive to changes in the effective pressure N in the ambient drainage system. This is far from true of the dynamic response of an isolated cavity to changes in N.

30 The dynamic response is of significant interest, as this is what a subglacial water pressure sensor would measure if connected to such an isolated cavity.

Here, I give three examples, in which the connected cavity in the lee of the larger bed protrusion (with $x_P = 1.64$) is forced periodically as shown in panels (b1-b3) of figure 9. The period and amplitude of the forcing pressure oscillation differs between
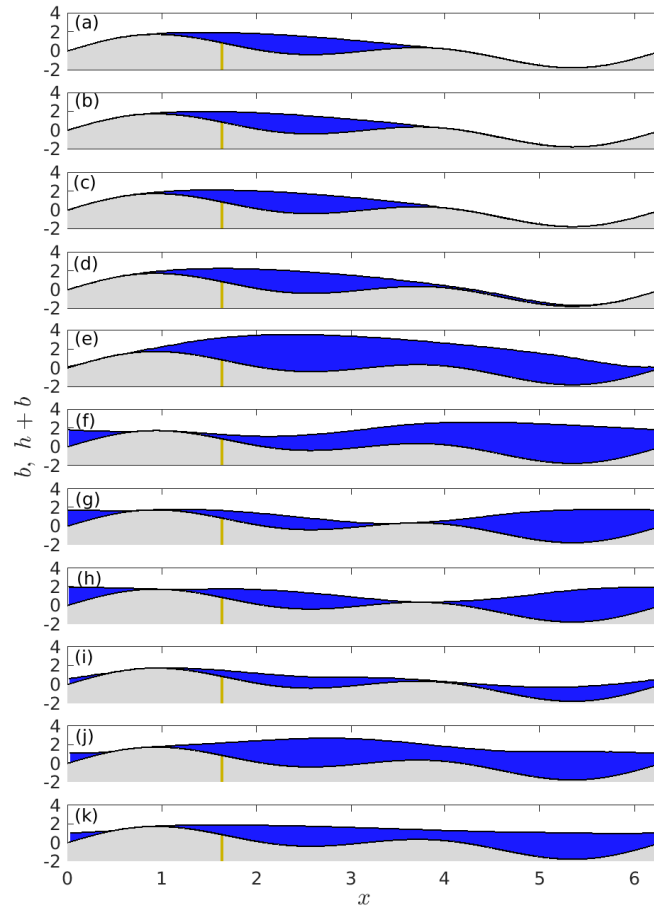
Figure 7. Cavity shapes for a step change from $N = 1.02$ to $N = 0.47$ (the blue curves in figure 6) at (a) $t = 0$, (b) $t = 5 \times 10^{-4}$, (c) $t = .32$, (d) $t = .49$, (e) $t = 1.35$, (f) $t = 3.39$, (g) $t = 4.62$, (h) $t = 5.16$, (i) $t = 6.61$, (j) $t = 8.70$ and (k) $t = 120$.

the columns of 9, with a period of π (column 1), 2π (column 2) and 4π (column 3). For reference, note that the advective period is $a/\bar{u} = 2\pi$. The green curves in panels (b1–b3) show that effective pressure N_M "measured" at the location marked M in panel (c). Note that the fixed location of M corresponds to a sensor installed at the glacier bed itself, which is unusual (Lefeuvre et al., 2015): in most field installations, pressure sensors are placed in boreholes and advected with the ice, corresponding to a location moving at velocity $\bar{u}$ in our model. Vertical grey lines in rows (a) and (b) correspond to times at which ice-bed contact is made or lost on the smaller bed protrusion upstream of N, while panels (a1–a3) show cavity end points as in figure 3(b).

In column 1, a relatively small isolated cavity forms before periodic behaviour is established. That cavity then remains isolated throughout the pressure cycle. The effective pressure N_M in that isolated cavity is in antiphase with the forcing effective pressure N in the connected cavity. This behaviour is familiar from field observations in parts of the glacier bed that
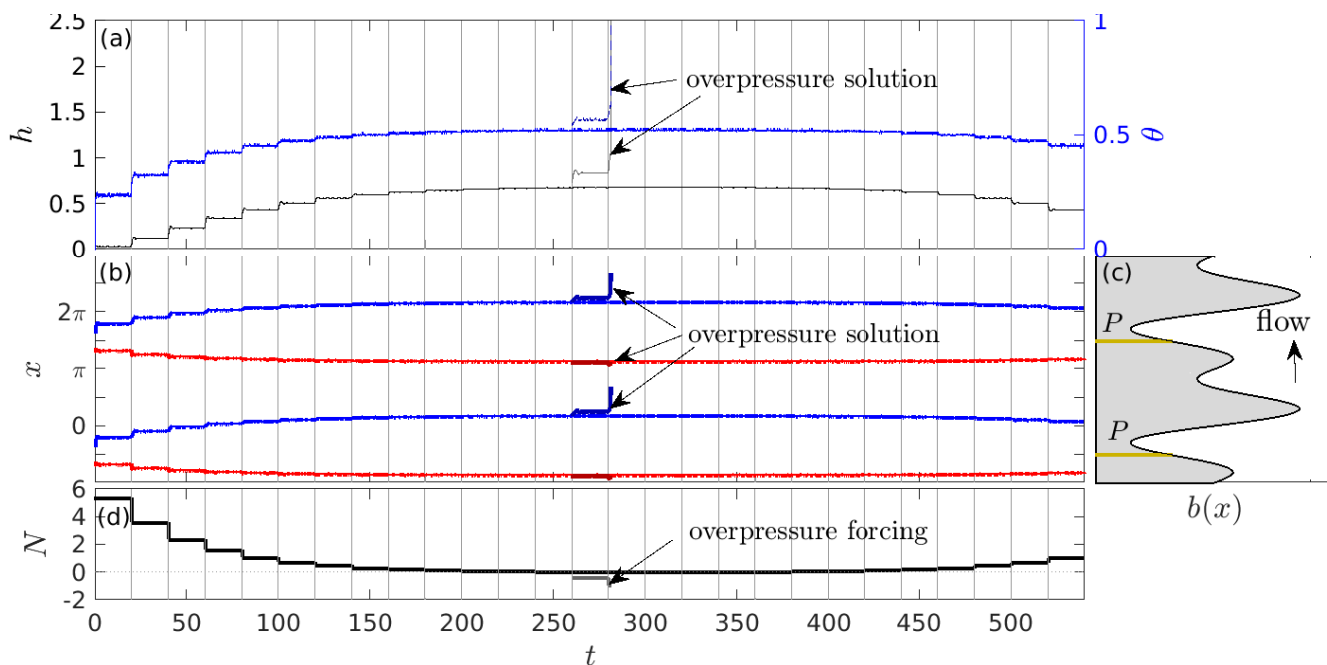
Figure 8. Using the same plotting scheme as in figure 3, dynamic cavity evolution under step changes in N with a permeable bed on the downstream side of the smaller bed protrusion, $P = \{./65\}$. The solution indicated by arrows corresponds to negative forcing effective pressure N, and departs from the solution not indicated by arrows at $t = 260$.

are not hydraulically connected (Murray and Clarke, 1995; Andrews et al., 2014; Lefeuvre et al., 2015; Rada and Schoof, 2018), and results from the need to maintain a fixed cavity volume.

When the forcing oscillations has a somewhat lower frequency (column 2), there are more significant changes in the ice-bed contact area on the smaller bed protrusion. An isolated cavity now forms during every other period of the forcing pressure oscillation (that is, the solution is periodic with a periodicty twice that of the forcing). In each case, the cavity roof makes contact with that protrusion after a maximum in N (panel (a)). For most of the intervals in which there is no contact on top of the smaller protrusion (see panel (a2)), the two effective pressures are nearly equal $N_M \approx N$ to a very close approximation. There is however a extended interval prior to contact being re-established, during which forcing effective pressure N is high and the "measured" effective pressure N_M drops below N. Even though the two cavities are connected across the top of the bed protrusion, the ice-bed gap width is narrow enough to support a significant pressure gradient. Once ice-bed contact is re-established, the measured effective pressure rapidly increases, and then goes through an antiphase pressure oscillation while the cavity around the point M is isolated. Once the connection between the cavities is re-established, the effective pressure at M rapidly equilibrates with that at P.

The forcing pressure oscillation in column 3 is even slower, and of larger amplitude than those in columns 1 and 2. Here, the solution has the same periodicity as the forcing, with a contact area forming on the smaller bed protrusion upstream of M
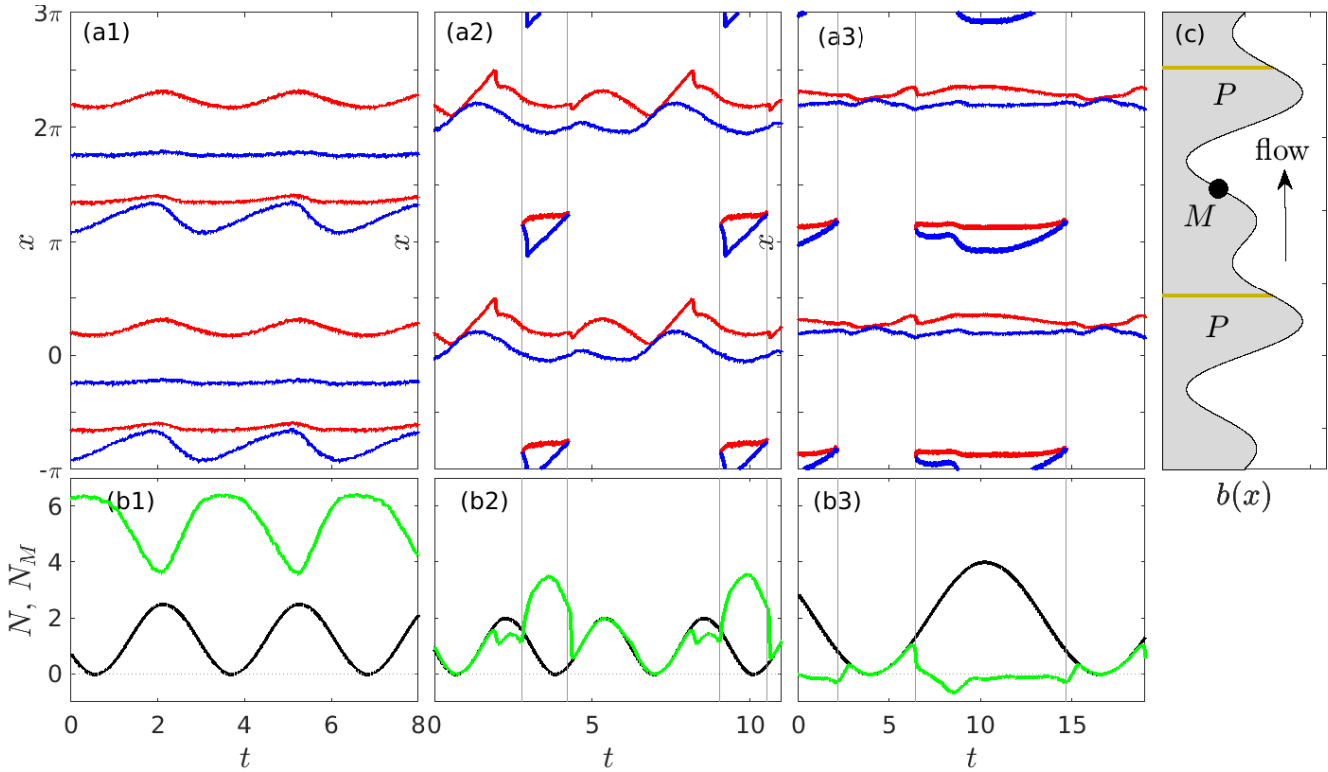
Figure 9. Using the same plotting scheme as in figure 3, dynamic cavity evolution under oscillatory forcing. Panel (a): time series of upstream (red) and downstream (blue) cavity end points. Vertical lines indicate when contact is made and lost with the smaller bed protrusion. Panel (b): corresponding bed geometry, permeable portion P indicated in beige. The circular black marker M indicates location where the effective pressure N_M is measured. Panel (c): time series of effective pressure N (black) and locally measured effective pressure (in green, given by the dimensionless variable $-p_w$ in the model) at the location of the black marker in panel (b).

when forcing effective pressure N is large. A reduced ice-bed gap size and consequent contact at the top of bed protrusions might be expected at large N, but contrasts with the solution in column 2 for a higher forcing frequency. As in column 2, $N_M \approx N$ when the cavities are connected, with a brief interval around $t = 15$ during which N_M is significantly lower than N after connection is re-established. Again, this results from a narrow ice-bed gap across the top of the smaller bed protrusion.

5   When the cavities become fully disconnected, N_M does not simply go through part of an antiphase pressure oscillation, unlike in column 2. After disconnection, N_M initially drops while N increases, with N_M reaching negative values. Subsequently, however, N_M rises again and relaxes to a near-zero value while the forcing effective pressure N is still increasing. It is tempting to ascribe the difference in behaviour between columns 2 and 3 to the slower period of forcing oscillation in column 3, and therefore to the greater ability of the solution to relax towards a steady state in column 3; given the long time scale for

10   relaxation to steady state that are evident in figure 3, it is unclear to what the extent that interpretation is appropriate.

4 Discussion

4.1 Subglacial hydrology

In part 1, I showed that for a steady-state model, connections between cavities are created and destroyed at critical values of N, and that the critical value for connection to a previously uncavitated part of the bed is lower than the critical value at which that

5 connection is closed, or at which a connection to a previously isolated cavity is established. The results in the present paper are consistent with these observations: figure 2 demonstrates that at $N = 1.0653$, hydraulic isolation of the downstream side of the smaller bed bump can be maintained in steady state (panel a). However, a single, larger cavity can equally extend across the top of the smaller bed bump at the same effective pressure (panel b), and the lee side of the smaller bed bump only becomes hydraulically isolated at higher effective pressures as in panel (c). A careful inspection of the final steady states in figures 3 and

10 4 will also confirm that connection to a previously uncavitated part of the bed happens at lower effective pressure (shortly after $t = 78$ in figure 4, at $N = 0.70$) than either subsequent isolation of part of the newly extended cavity (shortly after $t = 638$ in the same figure, at $N = 1.58$) reconnection (shortly after $t = 40$ in figure 4, at $N = 1.05$)

These insights are however misleading in a dynamic situation: figure 6 shows that the it is not the instantaneous drop in N below some critical value that causes a hydraulic connection to be established, but the subsequent growth of mean cavity depth

15 $\bar{h}$, averaged over the domain, and of the cavitation ratio θ (the fraction of the bed that is cavitated). In fact, θ reaching a critical value appears to be the best predictor for connection, though mean cavity depth $\bar{h}$ at connection varies by a relatively small amount, and it is plausible a critical value h_c could plausibly be defined.

This result at least is consistent with the previous modelling approach of Rada and Schoof (2018). Beyond that, matters become significantly more complicated: figure 6 pertains to a hydraulic connection being made by a cavity rapidly extending

20 past the top of a smaller bed bump, into a portion of the bed that was previously at low pressure but uncavitated. If that region subsequently becomes isolated again due to the cavity roof being lowered at increased N, the mean cavity depth $\bar{h}$ will remain larger than at the time the original connection was made, precisely because there is now a second cavity on the downstream side of the smaller bed bump (see figure 3(a)). In any case, we cannot use the same critical value h_c to determine whether there is a connection or not.

25 A plausible alternative to having a simple critical value h_c is to recognize that θ has also increased, and the definition of a critical value for connection should involve not only $\bar{h}$ but also θ. Doing so must then also reflect the observation in part 1, namely that connection to a previously uncavitated part of the bed happens at a lower critical effective pressure N than reconnection to a pre-existing isolated cavity: however the steady states of $\bar{h}$ and θ depend on N, the critical combination of $\bar{h}$ and θ that defines connection must be such that reconnection happens more easily than connection to an uncavitated part of

30 the bed.

These observations point to a need to extend drainage models to describe the evolution of not only $\bar{h}$, but also of at least one more independent state variable like θ. Note that $\bar{h}$ and θ are not simply proxies of each other (Gilbert et al., 2022): during the cavity connection events in figure 6, θ increases much faster than $\bar{h}$ initially, as a narrow ice-bed gap is formed (see also figure 7(d), and θ is clearly the more important measure of connectedness here.

Any attempt to amend subglacial hydrology models along these lines however faces another conundrum: as currently formulated, existing subglacial drainage models use an evolution equation for $\bar{h}$ of the generic first-order form (2), which is essentially a local ordinary differential equation (there being no spatial derivatives). The equation being first order in time, $\bar{h}$ should then monotonically relax to a stable steady state solution under conditions of constant sliding velocity u_b and effective
5   pressure N.

Figures 3, 4, 5 and 8 however all show $\bar{h}$ overshooting its steady state solution with an oscillatory approach to equilibrium. This is incompatible with (2): any dimensionally reduced representation of cavity evolution (relative to the full dynamic model developed in this paper) must involve more than one state variable. In a similar vein, the solution with time-dependent forcing in figure 9(b) shows a period doubling of the solution relative to the forcing. This is not necessarily incompatible with a model
10   of the form (2), but in typical implementations such as Werder et al. (2013), equation (2) is linear in $\bar{h}$, which does preclude period-doubling.

It is conceivable that a model of the form (2) could still be appropriate in many situations: the marked oscillations in figures 3, 4, and 5 are all associated with a single contact area per bed wavelength in a periodic bed, and there is a risk of numerical artifacts in some of these solutions due to only a handful of finite element nodes being in contact with the bed. Similarly,
15   the solution in figure 9(b) involves contact areas shrinking to very small sizes during the pressure cycles. The fact that the oscillations are minor when there is significant ice-bed contact or multiple contact areas, and the overshoot in $\bar{h}$ past its steady state value is generally small then suggests that the simple model (2) could capture cavity evolution well in the more realistic setting of an aperiodic bed. Further research using a more sophisticated approach to solving the model equations on larger domains with irregular beds would be needed to address this question.

20   If, on the other had, the overshoot oscillations are an important part of the evolution of the drainage system, then the set of variables that an extended model needs to consider is most likely larger than simply $(\bar{h}, \theta)$. As observed in figures 3 and 4, the oscillations in $\bar{h}$ seem to involve the contact area moving back and forth across the top of the most prominent bed bump while remaining of approximately constant size. That is, θ remains nearly constant during the oscillations. The addition of a dynamic variable θ while making v_o or v_c depend on θ is therefore unlikely to reproduce oscillatory behaviour, since θ should
25   be near-constant during the oscillations: a proxy for contact position rather than size appears to be necessary.

The ad hoc addition of dynamical variables is clearly a disturbing prospect in the absence of a clear roadmap for how closure should be achieved. Once a a set of such dynamical variables is identified, then perhaps the obvious next step would be to try to arrive at a closed set of equations for the evolution of these dynamical variables not by means of qualitative physical insight and subsequent parameter fitting, but by treating their evolution as being governed by a dynamical system that can be represented
30   by a neural network, which in turn can be trained on output from a detailed process-scale model such as that described here (e.g. Brenowitz and Bretherton, 2018, 2019). That procedure however still involves an expert choice of dynamical variables to use in the large scale model, and one would hope for something better: a method of optimally choosing these dynamical variables.

4.2 Interpretation of field measurements

The discussion above has focused on the implications of the local scale model results in the present paper for large-scale subglacial models. The same results also hold implications for the interpretation of field observations: a perhaps obvious consequence of hydraulic isolation of the bed is that the usual basal water pressure may no longer be smoothly varying in space, and in fact has no physical meaning in areas of ice-bed contact. For a highly permeable bed, a pressure sensor in a borehole that terminates on an ice-bed contact still measures the water pressure in any surrounding cavities, since water from those cavities can readily access the borehole through the bed. This is no longer true for an impermeable bed. Measuring borehole water pressure where a borehole terminates on an ice-bed contact area then records the peculiarities of pressure evolution in the isolated borehole, which itself is of unknown shape and must preserve its volume while subject to non-uniform stress field at the bed. The measurement in that situation no longer reflects conditions at the bed in a simple way.

By contrast, when a sensor is connected to an isolated cavity, the pressure measurement records the water pressure in the cavity. The latter again needs to preserve its own volume as modelled in the present paper. The pressure response of isolated cavities to temporally varying forcing pressures is sensitive to the time scales involved. For high-frequency oscillations in forcing (faster than the deformation time scale $a/\bar{u}$), the pressure response in isolated cavities is in antiphase with the forcing (figure 9(a1)), reflecting variations in the fraction of overburden supported by connected and isolated cavities. When forcing effective pressure N is low, a larger fraction of overburden is supported by the connected cavity, reducing normal stress on the isolated cavity, and therefore also reducing water pressure in the cavity, which corresponds to a higher effective pressure N_M (defined as overburden minus water pressure in the isolated cavity). Antiphase pressure oscillations of this type are familiar from observational records (Murray and Clarke, 1995; Lefeuvre et al., 2015; Rada and Schoof, 2018), and as shown by my results, do not require variations in ice velocity caused by the forcing effective pressure, since I have set sliding velocity to a constant (see also Lefeuvre et al., 2018).

For slower forcing oscillations, temporary connections between cavities can be established, corresponding to "switching events" observed in borehole pressure records (Hubbard et al., 1995; Rada and Schoof, 2018). During intervals of disconnection, the pressure response of the isolated cavity may again be in antiphase with forcing (figure 9(a2)), though this ceases to be the case during pressure oscillations that are significantly longer than the deformation time scale $a/\bar{u}$ (figure 9(a3)): in that case, the effective pressure during hydraulic disconnection does not satisfy any simple relationship with the forcing effective pressure, making interpretation of the recorded "data" challenging. Hydraulic connections between cavities can also be poor but not fully closed for extended intervals, as the result of small ice-bed gaps: these intervals most likely would not be interpreted as representing a hydraulic connection in observational data, and it is difficult to determine from the observed pressure time series when complete disconnection occurs.

4.3 Model improvements

There are likely to be many areas in which the model described here can be improved, ranging from a careful analysis of the numerical method used, to practical implementation issues such as the use of a potentially more suitable finite element basis,

adaptive time stepping and adaptive meshing as well effective parallelization. In addition, there are physical processes that the present work has been unable to consider.

The most obvious among the latter is the effective solution of the model in three dimensions to capture changes in hydraulic connectivity: in a two-dimensional model, it is impossible to establish connectivity from one end of the domain to the other unless ice-bed contact is lost everywhere, which is however not a physically reasonable situation. It is only in three dimensions that full end-to-end connectivity can coexist with continuing ice-bed contact. Similarly, I have focused purely on the hydrological aspects of dynamic cavity evolution and do not attempt to address the question of friction law for dynamically evolving subglacial cavities, which would be a worthwhile addition in its own right (de Diego et al., 2022; Gilbert et al., 2022), as would a consideration of non-constant viscosity in the ice. Lastly, the ability to capture flowing water through linked cavities in three dimensions would make the model a tempting test bed for studying spontaneous channelization at the process scale, by adding a term representing roof melting to the kinematic boundary conditions (9) or (13f) (see also Kamb (1987) and Dallaston and Hewitt (2014)). To avoid spuriously localized feedbacks between water depth and and dissipation-driven melting, it may then however be necessary to dispense with the simple local formula for water flux in terms of water depth as in (11b) by considering a horizontal turbulent viscosity (see also Creyts and Schoof, 2009).

5   Conclusions

In this paper, I have formulated a viscoelastic model for ice sliding over a rigid and mostly impermeable bed, allowing for the formation of cavities in which water is redistributed dynamically by an active local drainage system. The model is capable of describing the dynamic extension of subglacial cavities as bed obstacles progressively become submerged by water sourced from a localized water supply connected to an ambient drainage system at prescribed effective pressure. In the same vein, the model is capable of capturing the formation and evolution of isolated subglacial caviites that trap a fixed water volume after becoming isolated. Its steady state results agree well with the results of a simpler, two-dimensional and purely viscous steady state model that is solved by an entirely different numerical method.

The model lends some credence to existing approaches to modelling hydraulic isolation of the glacier bed in large-scale models using a threshold in mean cavity size to define connectivity, but also suggests that significant modifications to those models may be required. For instance, it suggests that the cavitation ratio measuring the horizontal extent of ice-bed separation needs to be considered separately from the mean ice-bed gap thickness, especially when modelling the rapid expansion of cavities as previously uncavitated low-pressure regions of the bed are flooded by water: cavitation ratio evolves faster, and is a better predictor of subglacial connectivity than ice-bed gap thickness, and the two variables are not simple proxies for one another (see also Gilbert et al., 2022). Adding the relevant physics to large-scale subglacial drainage model however requires the addition of model variables whose evolution is not described by an existing, simple parameterization, and future research needs to be directed towards constructing such parameterizations based on process model output.

Competing interests. The author declares no competing interests

Acknowledgements. This work was supported by NSERC Discovery Grant RGPIN-2018-04665 and by computing resources made available by the Department of Earth, Ocean and Atmospheric Sciences as well as the Digital Research Alliance of Canada.

References

Andrews, L., Catania, G., Hoffman, M., Gulley, J., Lüthi, M., Ryser, C., Hawley, R., and Neumann, T.: Direct observations of evolving subglacial drainage beneath the Greenland Ice Sheet, Nature, 514, 80–83, 2014.

Arnold, D., Brezzi, F., and Fortin, M.: A stable finite element for the Stokes equations, Calcolo, 21, 337–344, doi:10.1007/BF02576171, https://doi.org/10.1007/BF02576171, 1984.

Brenowitz, N. D. and Bretherton, C. S.: Prognostic Validation of a Neural Network Unified Physics Parameterization, Geophysical Research Letters, 45, 6289–6298, doi:https://doi.org/10.1029/2018GL078510, https://agupubs.onlinelibrary.wiley.com/doi/abs/10.1029/2018GL078510, 2018.

Brenowitz, N. D. and Bretherton, C. S.: Spatially Extended Tests of a Neural Network Parametrization Trained by Coarse-Graining, Journal of Advances in Modeling Earth Systems, 11, 2728–2744, doi:https://doi.org/10.1029/2019MS001711, https://agupubs.onlinelibrary.wiley.com/doi/abs/10.1029/2019MS001711, 2019.

Creyts, T. and Schoof, C.: Drainage through subglacial water sheets, J. Geophys. Res., 114, doi:10.1029/2008JF001 215, 2009.

Cuffey, K. and Paterson, W.: The Physics of Glaciers, Elsevier, Oxford, 4th edn., 2010.

Dallaston, M. and Hewitt, I.: Free-boundary models of a meltwater conduit, Phys. Fluids, 26, 0831 011–22, 2014.

Dash, J., Fu, H., and Wettlaufer, J.: The premelting of ice and its environmental consequences, Rep. Prog. Phys., 58, 115–167, 1995.

de Diego, G., Farrell, P., and Hewitt, I.: On the finite element approximation of a semicoercive Stokes variational inequality arising in glaciolog, arXiv, p. 2108.00046, 2021.

de Diego, G. G., Farrell, P. E., and Hewitt, I. J.: Numerical approximation of viscous contact problems applied to glacial sliding, Journal of Fluid Mechanics, 938, A21, doi:10.1017/jfm.2022.178, 2022.

Durand, G., Gagliardini, O., de Fleurian, B., Zwinger, T., and LeMeur, E.: Marine ice sheet dynamics: Hysteresis and neutral equilibrium, J. Geophys. Res., 114, doi:10.1029/2008JF001 170, 2009.

Fowler, A.: A theoretical treatment of the sliding of glaciers in the absence of cavitation, Phil. Trans. R. Soc. Lond., 298, 637–685, 1981.

Fowler, A.: A sliding law for glaciers of constant viscosity in the presence of subglacial cavitation, Proc. R. Soc. Lond. A, 407, 147–170, 1986.

Fudge, T., Humphrey, N., Harper, J., and Pfeffer, W.: Diurnal fluctuations in borehole water levels: configuration of the drainage system beneath Bench Glacier, Alaska, USA, J. Glaciol., 54, 297–306, 2008.

Gagliardini, O., Cohen, D., Raback, P., and Zwinger, T.: Finite-element modeling of subglacial cavities and related friction law, J. Geophys. Res., 112, F02 027, doi:10.1029/2006JF000 576, 2007.

Gilbert, A., Gimbert, F., Thøgersen, K., Schuler, T. V., and Kääb, A.: A Consistent Framework for Coupling Basal Friction With Subglacial Hydrology on Hard-Bedded Glaciers, Geophysical Research Letters, 49, e2021GL097 507, doi:https://doi.org/10.1029/2021GL097507, https://agupubs.onlinelibrary.wiley.com/doi/abs/10.1029/2021GL097507, e2021GL097507 2021GL097507, 2022.

Hammersley, J. and Welsh, D.: Percolation theory and its ramifications, Contemporary Physics, 21, 593–605, doi:10.1080/00107518008210661, https://doi.org/10.1080/00107518008210661, 1980.

Helanow, C., Iverson, N. R., Zoet, L. K., and Gagliardini, O.: Sliding Relations for Glacier Slip With Cavities Over Three-Dimensional Beds, Geophysical Research Letters, 47, e2019GL084 924, doi:https://doi.org/10.1029/2019GL084924, https://agupubs.onlinelibrary.wiley.com/doi/abs/10.1029/2019GL084924, e2019GL084924 10.1029/2019GL084924, 2020.

Helanow, C., Iverson, N. R., Woodard, J. B., and Zoet, L. K.: A slip law for hard-bedded glaciers derived from observed bed topography, Science Advances, 7, eabe7798, doi:10.1126/sciadv.abe7798, https://www.science.org/doi/abs/10.1126/sciadv.abe7798, 2021.

Hewitt, I.: Modelling distributed and channelized subglacial drainage: the spacing of channels, J. Glaciol., 57, 302–314, 2011.

Hewitt, I.: Seasonal changes in ice sheet motion due to melt water lubrication , Earth and Planetary Science Letters, 371, 16–25, 2013.

Hoffman, M., Andrews, L., Price, S., Catania, G., Neumann, T., Lüthi, M., Gulley, J., Ryser, C., Hawley, R., and Morris, B.: Greenland subglacial drainage evolutoin regulated by weakly connected regions of the bed, Nature Comms., 7, 13 903, 2016.

Hubbard, B., Sharp, M., Willis, I., Nielsen, M., and Smart, C.: Borehole water-level variations and the structure of the subglacial hydrological system of Haut Glacier d'Arolla, Valais, Switzerland, J. Glaciol., 41, 572–583, 1995.

Iken, A. and Bindschadler, R.: Combined measurements of subglacial water pressure and surface velocity of Findelengletscher, Switzerland: conclusions about drainage system and sliding mechanism, J. Glaciol., 32, 101–119, 1986.

Kamb, B.: Sliding motion of glaciers: Theory and observation, Rev. Geophys., 8, 673–728, 1970.

Kamb, B.: Glacier Surge Mechanism Based on Linked Cavity Configuration of the Basal Water Conduit System, J. Geophys. Res., 92, 9083–9100, 1987.

Kikuchi, N. and Oden, J.: Contact problems in elasticity : a study of variational inequalities and finite element methods, , SIAM, Philadelphia, 1988.

Lefeuvre, P.-M., Jackson, M., Lappegard, G., and Hagen, J. O.: Interannual variability of glacier basal pressure from a 20 year record, Annals of Glaciology, 56, 33–44, doi:10.3189/2015AoG70A019, 2015.

Lefeuvre, P.-M., Zwinger, T., Jackson, M., Gagliardini, O., Lappegard, G., and Hagen, J. O.: Stress Redistribution Explains Anti-correlated Subglacial Pressure Variations, Frontiers in Earth Science, 5, doi:10.3389/feart.2017.00110, https://www.frontiersin.org/articles/10.3389/feart.2017.00110, 2018.

Mitchell, S. L., Kuske, R., and Peirce, A. P.: An Asymptotic Framework for the Analysis of Hydraulic Fractures: The Impermeable Case, Journal of Applied Mechanics, 74, 365–372, doi:10.1115/1.2200653, https://doi.org/10.1115/1.2200653, 2006.

Murray, T. and Clarke, G.: Black-box modeling of hte subglacial water system, J. Geophys. Res., 100, 10 231–10 245, 1995.

Nye, J.: A calculation of the sliding of ice over a wavy surface using a Newtonian viscous approximation, Proc. R. Soc. Lond. A, 311, 445–467, 1969.

Rada, C. and Schoof, C.: Channelized, distributed and disconnected: subglacial drainage under a valley glacier in the Yukon, The Cryopshere, 12, 2609–2636, 2018.

Schoof, C.: The effect of cavitation on glacier sliding, Proc. R. Soc. Lond. A, 461, 609–627, doi:10.1098/rspa.2004.1350, 2005.

Schoof, C.: The evolution of isolated cavities and hydraulic connection at the glacier bed. Part 1: steady states and friction laws, The Cryosphere, submitted.

Schoof, C., Hewitt, I., and Werder, M.: Flotation and free surface flow in a model for subglacial drainage. Part 1. Distributed drainage, J. Fluid Mech., 702, 126–156, 2012.

Sommers, A., Rajaram, H., and Morlighem, M.: SHAKTI: Subglacial Hydrology and Kinetic, Transient Interactions v1.0, Geoscientific Model Development, 11, 2955–2974, doi:10.5194/gmd-11-2955-2018, https://gmd.copernicus.org/articles/11/2955/2018/, 2018.

Spence, D. A., Sharp, P., and Benjamin, T. B.: Self-similar solutions for elastohydrodynamic cavity flow, Proceedings of the Royal Society of London. A. Mathematical and Physical Sciences, 400, 289–313, doi:10.1098/rspa.1985.0081, https://royalsocietypublishing.org/doi/abs/10.1098/rspa.1985.0081, 1985.

Stubblefield, A. G., Spiegelman, M., and Creyts, T. T.: Variational formulation of marine ice-sheet and subglacial-lake grounding-line dynamics, Journal of Fluid Mechanics, 919, A23, doi:10.1017/jfm.2021.394, 2021.

Thøgersen, K., Gilbert, A., and Schuler, T.: Rate-and-state friction explains glacier surge propagation, Nat. Comms., 10, 2023, doi:10.1038/s41467-019-10506-4, https://doi.org/10.1038/s41467-019-10506-4, 2019.

5 Touvet, T., Balmforth, N., Craster, R., and Sutherland, B.: Fingering instability in buoyancy-driven fluid-filled cracks, Journal of Fluid Mechanics, 672, 60–77, doi:10.1017/S0022112010005860, 2011.

Tsai, V. and Rice, J.: A Model for Turbulent Hydraulic Fracture and Application to Crack Propagation at Glacier Beds, J. Geophys. Res., 115, doi:10.1029/2009JF001 474, 2010.

Tsai, V. C. and Rice, J. R.: Modeling Turbulent Hydraulic Fracture Near a Free Surface, Journal of Applied Mechanics, 79,
10 doi:10.1115/1.4005879, https://doi.org/10.1115/1.4005879, 031003, 2012.

Warburton, K., Hewitt, D., and Neufeld, J.: Tidal grounding line migration modulated by subglacial hydrology, Geophys. Res. Lett., 47, e2020GL089 088, doi:10.1029/2020GL089088, https://doi.org/10.1029/2020GL089088, 2020.

Weertman, J.: On the sliding of glaciers, J. Glaciol., 3, 33–38, 1957.

Werder, M., Hewitt, I., Schoof, C., and Flowers, G.: Modeling channelized and distributed subglacial drainage in two dimensions, J. Geophys.
15 Res., F118, 2140–215, doi: 10.1002/jgrf.20 146, 2013.

Zarrinderakht, M., Schoof, C., and Peirce, A.: The effect of hydrology and crevasse wall contact on calving, The Cryosphere, 16, 4491–4512, doi:10.5194/tc-16-4491-2022, https://tc.copernicus.org/articles/16/4491/2022/, 2022.